Unraveling the oxygen vacancy structures at the reduced $CeO_2(111)$ surface

Zhong-Kang Han,[1,2,*] Yi-Zhou Yang,[1,2] Beien Zhu,[1] M. Verónica Ganduglia-Pirovano,[3,†] and Yi Gao[1,4,‡]

[1]*Division of Interfacial Water and Key Laboratory of Interfacial Physics and Technology, Shanghai Institute of Applied Physics, Chinese Academy of Sciences, 201800 Shanghai, China*

[2]*University of Chinese Academy of Sciences, 100049 Beijing, China*

[3]*Instituto de Catálisis y Petroleoquímica, Consejo Superior de Investigaciones Científicas, Marie Curie 2, 28049 Madrid, Spain*

[4]*Shanghai Science Research Center, Chinese Academy of Sciences, 201204 Shanghai, China*

(Received 5 April 2017; revised manuscript received 11 September 2017; published 14 March 2018)

Oxygen vacancies at ceria (CeO_2) surfaces play an essential role in catalytic applications. However, during the past decade, the near-surface vacancy structures at $CeO_2(111)$ have been questioned due to the contradictory results from experiments and theoretical simulations. Whether surface vacancies agglomerate, and which is the most stable vacancy structure for varying vacancy concentration and temperature, are being heatedly debated. By combining density functional theory calculations and Monte Carlo simulations, we proposed a unified model to explain all conflicting experimental observations and theoretical results. We find a novel trimeric vacancy structure which is more stable than any other one previously reported, which perfectly reproduces the characteristics of the double linear surface oxygen vacancy clusters observed by STM. Monte Carlo simulations show that at low temperature and low vacancy concentrations, vacancies prefer subsurface sites with a local (2×2) ordering, whereas mostly linear surface vacancy clusters do form with increased temperature and degree of reduction. These results well explain the disputes about the stable vacancy structure and surface vacancy clustering at $CeO_2(111)$, and provide a foundation for the understanding of the redox and catalytic chemistry of metal oxides.

DOI: 10.1103/PhysRevMaterials.2.035802

I. INTRODUCTION

Ceria (CeO_2) is a key component in catalysts for automotive exhaust treatment, production and purification of hydrogen, oxidative dehydrogenation, and many other applications, with the reducibility of the system being crucial for its function in such applications [1–8]. Surface oxygen vacancies are the most relevant ceria defects that may not only act as anchoring sites for catalytically active metal species, but also influence the structure and charge of supported metal clusters, which in turn influence catalytic activity [7,9–19]. The knowledge of the defect structure of ceria surfaces is therefore crucial toward the fundamental understanding of the reactivity of ceria-based systems. Consequently, oxygen defects at the reduced $CeO_2(111)$ surface have been widely studied by scanning tunneling microscopy (STM) [20–24], dynamic force microscopy (DFM) [22,25–28], and density functional theory (DFT) calculations [20,24,28–42]. In 2005, Esch *et al.*'s seminal work [24] presented high-resolution STM images at high temperature, leading to three major observations: (1) On the moderately reduced surface, isolated single surface oxygen vacancies (SSVs) and subsurface ones (SSSVs) are both abundant with comparable percentages, indicating a similar stability between the vacancy species, whereas the surface vacancies agglomerate with increasing degree of reduction. (2) First-neighbor surface oxygen vacancies form predominantly linear clusters (LSVCs) along with some triangular trimers (SVTs), which suggests that linear arrangements are more stable than triangular ones. (3) Subsurface vacancies are essential for LSVC nucleation. Thus, for example, a double linear surface vacancy cluster (dLSVC) consists of three first-neighbor vacancies, namely, two SSVs and one SSSV. The key feature of all the linear clusters observed in the STM is the existence of a pair of rim O atoms that face each other, which are both laterally shifted toward the inside of the defect as well as vertically displaced from the unperturbed surface, one above and one below. Yet, this breakthrough work initiated a decade of heated debate on whether surface vacancies agglomerate (see Table 1). In contrast to Esch *et al.*'s STM results [24], Torbrügge *et al.* [27] employed DFM and observed mostly subsurface vacancies on the slightly reduced $CeO_2(111)$ surface at 80 K, with a (2×2) local ordering. Moreover, Ganduglia-Pirovano *et al.* [34] and Li *et al.* [35] carried out DFT calculations and showed that isolated subsurface vacancies are more stable than surface ones with multiple local minima with respect to the sites on which the excess electrons—driving the $Ce^{4+}(4f^0)$ to $Ce^{3+}(4f^1)$ reduction—localize, the existence of which has been asserted in the STM study by Jerratsch *et al.* [20]. Furthermore, recent DFT work by Murgida *et al.* [40] stands out in evidencing the high stability of a (2×2) ordered subsurface vacancy structure. As yet, the studies of surface vacancy aggregates are relatively scarce and with contradictory results about the interactions between vacancies [15,24,25,33,37,38,43]. Few works explicitly reported on the surface vacancy-vacancy interaction [37,38], among which all but one [38] found it repulsive, hence

*Present address: Fritz Haber Institute of the Max Planck Society, Faradayweg 4-6, 14195 Berlin, Germany.

†vgp@icp.csic.es

‡gaoyi@sinap.ac.cn

TABLE I. List of experimental and theoretical debated results about the near-surface vacancy structures at the reduced $CeO_2(111)$ surface and their relative stability. SSV, SSSV, SVT, dLSVC, and ms-dLSVC stand for single surface vacancy, single subsurface vacancy, surface vacancy trimer, double linear surface vacancy cluster, and most stable double linear surface vacancy cluster, respectively (cf. Fig. 1). Θ: Concentration. T: Temperature.

	Stable vacancy structure	Relative stability linear vs triangular surface vacancy structures	Pairing features of oxygen ions neighboring linear vacancy
Experiment			
Esch's STM (573–673 K) [24]	Moderately reduced: Isolated SSVs and SSSVs Highly reduced: Linear and triangular clusters	linear > triangular	YES
Torbrügge's DFM (80 K) [27]	Slightly reduced: SSSVs → (2 × 2) ordered structure	–	–
Theory			
Oxygen vacancies [33–35,37,40,43,45]	SSSVs → (2 × 2) ordered structure SSVs→ repulsive interaction	SVT (triangular)> dLSVC (linear)	NO
F-surface impurity model [44,48]	F impurities agglomerate 300 K, $\Theta = 5\%-15\%$: compact structures 600–900 K, $\Theta = 5\%-15\%$: open clusters	triangular > linear linear > triangular	NO
OH model [45–47]	SSVs + H_{sub} agglomerate	linear > triangular	NO
This work			
Oxygen vacancies	Low T, low Θ: SSSVs→ (2 × 2) ordered structure High T, high Θ: Linear and triangular clusters	ms-dLVC (linear) > SVT (triangular)	YES

theoretical studies are inconsistent with the STM observations by Esch *et al.* [24]. Even more confusion resulted from the contradictions between experiments and calculations concerning the relative stability between linear- and triangular-shaped surface vacancy aggregates [15,24,25,33,43]. All calculations [15,33,43] predicted that SVTs are by about 0.5 to 1.0 eV more stable than dLSVCs, against the experimental observations [24].

Recently, in order to explain the surface defect clustering (cf. Table I), new models were theoretically proposed [44–48]. Kullgren *et al.* [44,48] suggested that the observed surface defects were fluorine impurities, but did not address the existence of subsurface defects. Moreover, the most recent DFT calculations show that triangular fluorine trimers are more stable than linear ones by ∼0.05 eV [48], although Monte Carlo simulations show a change from more compact to linear-shaped fluorine aggregates for impurity concentrations of 5% to 15% as the temperature increases from 300 to 600 K [48]. Another suggestion is that of the hydroxyl-vacancy model proposed by Wu *et al.* [45–47], which predicts that isolated surface oxygen vacancies aggregate in the presence of subsurface hydroxyl species, with linear structures being more stable than triangular ones. More importantly, both fluorine impurity and hydroxyl-vacancy models cannot reproduce the above-mentioned particular topological features of the STM images of the linear defect structures [24]. Until now, there is not a unique model consistent with all the key findings in Esch *et al.*'s STM and Torbrügge *et al.*'s DFM experiments as well as the existing theoretical results.

In this work we explain all conflicting experimental observations and theoretical results by combining density functional theory calculations and Monte Carlo simulations. We consider different oxygen vacancy structures—including surface and subsurface sites—and locate a new double linear surface oxygen vacancy structure as the most stable trivacancy cluster (ms-dLSVC) that is more stable than a triangular-shaped one and perfectly reproduces the key features in every LSVCs imaged by STM [24]. Moreover, Monte Carlo simulations show that vacancy concentration and temperature are essential factors to explain the stability of the observed subsurface vacancies with third-nearest-neighbor distance [27], as well as the formation of first-neighbor linear surface vacancy aggregates [24]. These findings solve the decade mystery about the defect structure of the reduced $CeO_2(111)$ surface without any assumption such as the existence of impurities, and provide support for the interpretation of the most recent experimental results [24,27].

II. METHODS

The spin-polarized DFT calculations were carried out using the generalized gradient approximation (GGA) of Perdew-Burke-Ernzerhof (PBE) as implemented in the VASP code [49,50]. The DFT+U methodology [51,52] with an effective U value of 5.0 eV was used to describe the localized Ce $4f$ states (Ce^{3+}), which is within the range of suitable values to describe reduced ceria-based systems [53]. We used projector-augmented wave (PAW) potentials [54] with Ce ($4f$, $5s$, $5p$, $5d$, $6s$) and O ($2s$, $2p$) electrons as valence states, and a plane-wave cutoff of 400 eV. To locate the minimum energy structure for different types of near-surface oxygen vacancy clusters, numerous possible electronic configurations were considered (Fig. S1 and Table S1 of the Supplemental Material [55]). In view of the hundreds of configurations to be sampled, the $CeO_2(111)$ surface was firstly modeled by $p(5 \times 5)$ unit cells and three O–Ce–O trilayers (TL) separated by 15 Å

TABLE II. Average oxygen vacancy formation energy E_s^a for SVT, SVT2, dLSVC, and ms-dLSVC on $CeO_2(111)$ surface. Values are calculated for a $p(6 \times 6)$ supercell with different number of trilayers (TL), sampling of the reciprocal space (k-points), and energy cutoff.

	E_s^a (eV/atom)			
	Γ point			2×2×1 k-points
Type	400 eV; 3 TL[a]	500 eV; 3 TL	400 eV; 4 TL	400 eV; 3 TL
SVT	2.16	2.15	2.14	2.16
SVT2	2.22	2.21	2.20	2.22
dLSVC	2.63	2.63	2.61	2.62
ms-dLSVC	2.01	2.01	1.99	2.02

[a]This computational model and setup was chosen in all calculations of the lowest-energy structures of single vacancies and vacancy clusters. Unless otherwise noted, all the energy values reported in the main text of this paper are obtained using this setup.

vacuum space to avoid interaction between periodic images. Due to the large supercell dimensions, the k-point sampling was restricted to the Γ point. In all geometry optimizations, all atoms in the bottom CeO_2 TL were fixed to their bulk-truncated positions, whereas the rest of the atoms were allowed to fully relax. Next, for the lowest-energy Ce^{3+} configuration for each vacancy distribution, additional calculations using a 3 TL slab with a $p(6 \times 6)$ supercell and the Γ point were performed (cf. Table S2 [55]). Moreover, in order to confirm the robustness of the model and computational setup, selected calculations were carried out employing a thicker 4 TL slab or a larger k-mesh ($2 \times 2 \times 1$ k-points) or a larger cutoff of 500 eV, see Table II. The STM images were calculated according to the Tersoff-Hamman model [56].

In order to determine the ground-state configuration of oxygen vacancies as a function of concentration and temperature at the $CeO_2(111)$ surface, the Monte Carlo method was applied to a cluster-expansion model Hamiltonian [57], which was parametrized using the energies of a set of 31 clusters (Figs. S1 and S2, and Table S2 [55]) computed by DFT calculations, employing a slab with $p(6 \times 6)$ periodicity, 3 CeO_2 trilayers, and the Γ point. The energy E_s of a configuration s is described as $E_s = \sum_{a=1}^{N_a=31} m_a J_a X_{sa}$ where the sum is taken over all symmetrically inequivalent interactions (clusters). The multiplicities m_a indicate the number of clusters that are equivalent by symmetry to α and J_a are the effective cluster interactions (the J_a parameters (in eV) of the set of 31 clusters (Fig. S1) are collected in Table S3 [55]). The values of X_{sa} are the probability of finding the cluster a in the configuration s. For example, for the configuration s as shown in Fig. S3 [55], the probability of finding the clusters J_1 in Fig. S1(a), J_3 in Fig. S1(c), and J_9 in Fig. S1(i) [55] are $X_{s1} = 3/36$ (actual number of single surface vacancies divided by the total possible number of isolated vacancies), $X_{s3} = 1/36$ (actual number of symmetrically nonequivalent surface vacancy dimers divided by the total possible number of dimers), and $X_{s9} = 1/36$ (actual number of trimers divided by the total possible number of trimers), respectively, and the probability of finding all the other clusters are zero. (For example, the probability of finding the single subsurface cluster J_2 in Fig. S1(b) [55] is 0. Thus $X_{s2} = 0$.) The corresponding values of J_a are $J_1 = 75.703$ eV, $J_3 = 2.121$ eV, and $J_9 = -0.019$ eV, respectively, and those of m_a are $m_1 = 1$ (a single surface vacancy has one orientation), $m_3 = 3$ (a surface vacancy triangle consists of three differently oriented, but symmetrically equivalent, surface vacancy dimers), and $m_9 = 1$ (a surface vacancy triangle has one orientation), respectively. Thus, the predicted ground-state energy for this configuration is $E_s = m_1 J_1 X_{s1} + m_3 J_3 X_{s3} + m_9 J_9 X_{s9} = 6.48$ eV, and the predicted average oxygen vacancy formation energy is $\Delta E_s^a = E_s/3 = 2.16$ eV, which compares nicely with the true DFT-calculated average oxygen formation energy, i.e., $\Delta E_{\mathrm{DFT}}^a = 2.16$ eV. For more details, see Ref. [56]. The mean square error of the cluster expansion model is about 0.01 eV, which shows that the model has a low overall error (cf. Table S2 [55]). As shown in Fig. S5 and Table S4, the predicted lowest average oxygen vacancy formation energies (ΔE_{ce}^a) for a set of selected configurations are very well consistent with the corresponding DFT-calculated values ($\Delta E_{\mathrm{DFT}}^a$), which shows the reliability of the cluster expansion model [55]. For the Monte Carlo simulations, a 2D-periodic network consisting of two layers of 50×50 sites was employed. Each site was occupied by either an O atom or an O vacancy. Each trajectory with five million trial steps, starting from random states, were simulated using the METROPOLIS algorithm [58] for a varying fraction of near-surface vacant sites at a given temperature, as specified below.

III. RESULTS

It is known that the excess charge localization highly influences the relative stabilities of near-surface oxygen vacancy structures. Thus, in this study, different Ce^{3+} configurations were considered for a given vacancy distribution of monomers, dimers, and trimers (Fig. S1 and Table S1 [55]). The most stable single surface vacancy (SSV) and single subsurface vacancy (SSSV) structures have the two excess electrons localized on next-nearest-neighbor cerium positions relative to the vacancy sites [Figs. 1(a) and 1(b), respectively], where SSSV is lower in energy by 0.18 eV (cf. 1.91 and 2.09 eV for SSSV and SSV vacancy formation energies, respectively), in good agreement with previous calculations [59].

For trivacancy clusters, the SVT [Fig. 1(c)] and dLSVC [Fig. 1(d)] structures were initially proposed by Esch *et al.* [24] to explain their observed STM images of triangular and double linear surface oxygen vacancy aggregates. The

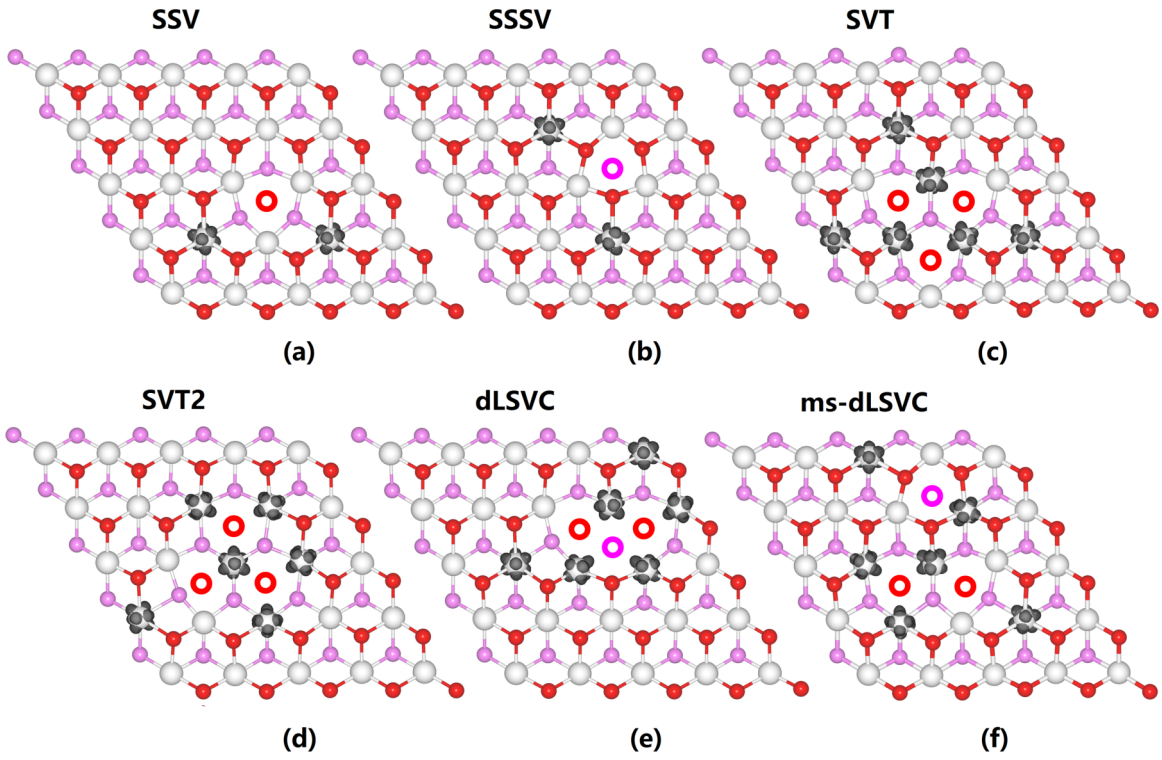

FIG. 1. Most stable single vacancy and trimeric vacancy structures on $CeO_2(111)$. Isolated vacancy: (a) surface (SSV) and (b) subsurface (SSSV). Triangular shaped: (c) SVT and (d) SVT2, and linear shaped: (e) dLSVC and (f) ms-dLSVC. Cerium, surface oxygen, and subsurface oxygen atoms are depicted in white, red, and pink, respectively. Open circles represent oxygen vacancies. Cerium, surface oxygen, and subsurface oxygen atoms are depicted in white, red, and pink, respectively. Open circles represent oxygen vacancies. For clarity, only the first O–Ce–O trilayer (TL) is shown. The spin density is shown as the gray clouds localized on cerium cations.

calculated average vacancy formation energies E_s^a are used to estimate the stability of different oxygen vacancy clusters which are collected in Table II and Table S1 [55]. Here $E_s^a = (E_{\text{slab}}^n - E_{\text{slab}}^{\text{stoi}} + \frac{n}{2}E_{O_2})/n$, where E_{slab}^n, $E_{\text{slab}}^{\text{stoi}}$, and E_{O_2} are the total energies of the reduced surface with n oxygen vacancies, the clean stoichiometric surface, and the gas-phase O_2 molecule, respectively. Our calculations show that dLSVC has a 0.47 eV/atom larger formation energy than SVT (Table II), consistent with previous findings [33,43]. However, the results contradict the observation in the high resolution STM images by Esch *et al.* [24], where dLSVC aggregates are much more frequent than SVTs. Given that the subsurface oxygen vacancy species involved in the formation of linear surface oxygen vacancy clusters (LSVCs) could not be directly observed in the STM experiments, we explored all possible arrangements for three neighboring near-surface vacancies—and many configurations for the excess charge—and found that a structure with two first-neighbor surface oxygen vacancies and a subsurface vacancy at a fifth-neighbor distance within the oxygen sublattice of bulk ceria [Fig. 1(f)], is the most stable trimeric structure (Table S2 [55]), hereafter labeled ms-dLSVC (most stable double linear surface vacancy cluster). The ms-dLSVC has never been reported before and is more stable than the triangular-shaped SVT by 0.15 eV/atom (Table II). The higher stability of the ms-dLSVC with respect to the SVT structure can be attributed to vacancy-induced lattice relaxation effects, which relate to the larger distance between vacancies in the linear structure as well as the predominant occupation of next-nearest-neighbor sites to the vacancies by the excess electrons (cf. Fig. 1). The energy required to create the unrelaxed ms-dLSVC structure by cutting Ce–O bonds of the clean $CeO_2(111)$ surface is larger than that to construct the unrelaxed STV by 0.37 eV/atom. In the former case, more Ce–O bonds are cut due to the presence of a subsurface vacancy. However, the ms-dLSVC structure has the largest energy gain of 1.92 eV/atom due to lattice relaxations, compared to 1.40 eV/atom for SVT, which causes that ms-dLSVC has 0.15 eV/atom energy preference compared to SVT (Table II). It should be noted that besides the SVT structure with the center on a subsurface oxygen atom, there is another SVT configuration with the center on a cerium atom [Fig. 1(d)], we term it as SVT2. However, experimental observations did not point to the presence of SVT2-type clusters [24], which is consistent with our results that the SVT is more stable than the SVT2 by 0.18 eV.

To reveal whether the new-found ms-dLSVC structure is consistent with the observed particular topological features of the STM images of linear vacancy structures [24], atom positions and simulated STM images were analyzed. In Fig. 2 we show that the ms-dLSVC structure nicely reproduces the experimental observations with a pair of O atoms vertically relaxing, one inward by −0.13 Å (magenta ball/arrow) and the other one outward by +0.15 Å (cyan ball/arrow), in remarkable agreement with the STM results [24]. We note that in the lowest-energy configurations of the trimeric dLSVC (first neighbor subsurface vacancy) and dimeric (no subsurface

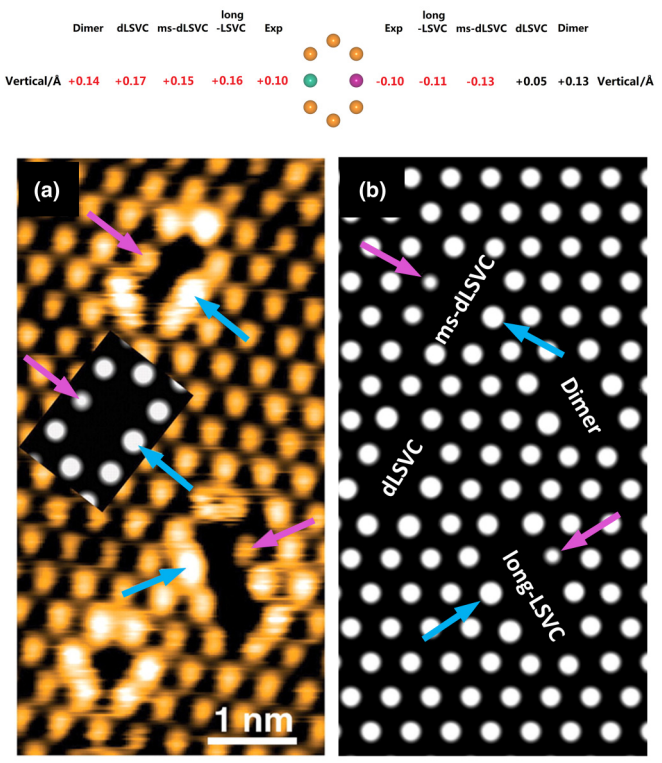

FIG. 2. Top panel: Vertical displacement of surface O atoms in SVCs. Schematic representations of the vertical movement of the oxygen atom pair formed by the cyan and magenta atoms upon formation of vacancy clusters, namely, dimer, dLSVC, ms-dLSVC, and long-LSVC. The outward and downward relaxations are denoted with + or − signs, respectively. Values consistent with experimental observation are highlighted in red. Bottom panel: Experimental image of Ref. [24] (a) and simulated (b) STM images of vacancy structures on reduced $CeO_2(111)$. The height of the tip in the constant-height mode simulated images is ∼0.6 Å. The insert in (a) displays the simulated STM image of the dLSVC structure by Esch *et al.* with all Ce^{3+} ions in nearest-neighbor positions to the vacancies [24]. Experimental STM image reprinted with permission from Esch *et al.*, Science **309**, 752 (2005). Copyright 2005, American Association for the Advancement of Science.

vacancy) structures, both oxygen atoms relax outward [cf. Fig. 2; +0.05 Å and +0.17 Å (dLSVC), and +0.13 Å and +0.14 Å (dimer)]. Note that a dLSVC configuration with all Ce^{3+} ions in nearest-neighbor positions to the vacancies, such as that proposed by Esch *et al.* [24], is about 0.1 eV/atom higher in energy than the one here considered (Table S1 [55]), although it is characterized by one O atom relaxing inward by −0.08 Å and the other outward by +0.12 Å (cf. −0.07 and +0.10 Å, respectively, in Ref. [24]). Moreover, the STM simulation of a longer LSVC (long-LSVC) cluster with the removal of an additional surface oxygen atom from ms-dLSVC (Fig. S6 [55]) also perfectly reproduces the characteristic oxygen pair unit (Fig. 2) observed in every long LSVC imaged by Esch *et al.* [24]. At the same time, it is important to stress that the STM simulations of the previously proposed models for double surface defects, i.e., the fluorine impurity [44] and the hydroxyl-vacancy [45] models, are not fully consistent with the experimental observations, as no special relaxation pattern of the O atoms around a defect border can be reproduced (Fig. S7 [55]).

Isolated single subsurface vacancies are known to repel each other [40] and thus we consistently found that dimeric as well as linear and triangular trimeric structures with first neighboring subsurface vacancies are less stable than having corresponding isolated species by 0.11 eV/atom for the dimer and 0.12 eV/atom for the trimers (cf. Fig. S1d, z2, z5, and Table S2 [55]). At low temperatures and vacancy concentrations, vacancies are expected to occupy mostly the subsurface with a (2 × 2) local ordering [40]. However, at somewhat higher temperatures and concentrations, clusters will inevitably form and ms-dLSVC, as the most stable cluster structure with respect to 2 SSVs and 1 SSSV (by 60 meV), should be more frequently observed. Here it should be noted that the statement is robust with respect to the existence of higher-energy electronic configurations. Specifically, E_s^a for the higher-energy electronic configurations of the ms-dLSVC structure lie within the 2.04–2.12 eV/atom energy range, notably lower in energy than the values for isolated single surface and subsurface species that lie within the 2.14–2.29 eV/atom and 2.10–2.22 range, respectively (Table S1 [55]). Hence, ms-dLSVC-type structures should indeed preferentially form.

To further explain the subsurface vacancy repulsion and surface vacancy clustering in experimental observations [24,27], as mentioned above, we performed Monte Carlo simulations of the reduced surface with different near-surface vacancy concentrations (10%, 15%, and 20%, i.e., a slight, moderate, and high degree of reduction, respectively) and varying temperature such as 80 K (same as in the DFM experiment by Torbrügge *et al.* [27]) and 600 K (same as in the STM experiment by Esch *et al.* [24]), based on our DFT results (Table S2 [55]). Figures 3(a) and 3(d) display the MC simulated vacancy structure for 10% vacancies. The 80 K simulation gives an ideal vacancy distribution [Fig. 3(a)] for the slightly reduced surface where isolated vacancies are located in the subsurface, forming third-neighbor vacancy pairs and (2 × 2) locally ordered patches, fully consistent with recent DFT predictions [40] and experimental observations by Grinter *et al.* [21] and Torbrügge *et al.* [27] for slightly reduced $CeO_2(111)$ surfaces at low temperature. Heating a not too much reduced $CeO_2(111)$ surface to elevated temperature [Fig. 3(d)] results in the appearance of surface vacancies.

Up to a total concentration of 15% of near-surface vacancies [Figs. 3(b) and 3(e)], most surface vacancies are isolated, however, some vacancy clustering into mostly short linear clusters is observed. These clusters are of the ms-dLSVC type since a fifth-neighbor subsurface vacancy is involved in their formation [Figs. 3(b) and 3(e)], and the observed structure agrees well with the experimental findings by Esch *et al.* [24]. For higher degrees of reduction such as 20%, a great number of vacancy clusters appears [Figs. 3(c) and 3(f)], mostly linear (LSVCs) but also some triangular shaped. The long LSVCs appear in three different orientations, reflecting the threefold symmetry of the substrate. Almost all of the LSVCs involve a fifth-neighbor subsurface vacancy as in the ms-dLSVC clusters, which can reproduce the special relaxation pattern of O atoms around the defects in the STM images by Esch *et al.* [24]. The next abundant surface vacancy species after LSVCs are SVTs with the center on a subsurface

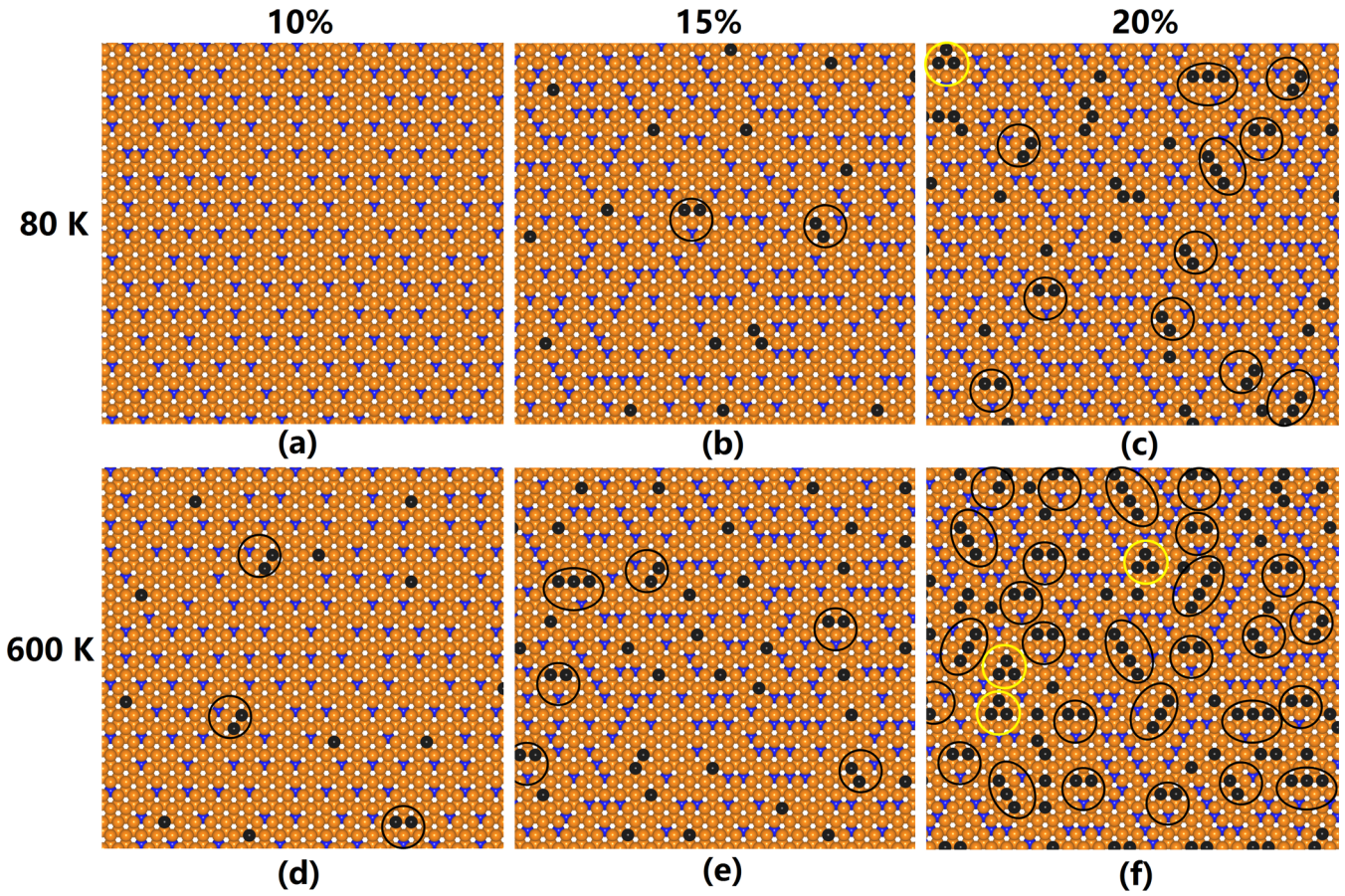

FIG. 3. Monte Carlo simulated structures of a slightly (10%), moderately (15%), and highly (20%) reduced CeO_2(111) surface. (a)–(c) 80 K and (d)–(f) 600 K. Images are to be compared with the experimental STM images in Ref. [24] (Figs. 1(a) and 1(b)). Oxygen atoms, surface oxygen vacancies, and subsurface oxygen vacancies are represented as orange, black, and blue balls, respectively. Cerium atoms are not shown for clarity. The ms-dLSVCs and long LSVCs are indicated with the black circles. The SVTs are indicated with the yellow circles.

oxygen atom. These results are perfectly consistent with the STM experiments [24]. It should be noted that the kinetic behavior of oxygen vacancies can also be crucial to the properties of ceria systems as exemplified by the case of the CeO_2(100) surface [60] and bulk ceria [61]. However, the previous STM and DFM studies are focused on the thermodynamic equilibrium structures of the reduced CeO_2(111) surface [24,27]. Thus, in our MC simulations the kinetic part is not included.

IV. SUMMARY

In summary, we employed the DFT+U method and Monte Carlo simulations to provide firm theoretical support for the interpretation of the various experimental results and help solve the long-time debate about the surface oxygen vacancy structure between experiments and calculations. Our results provide the foundations for understanding the nucleation of surface vacancies on ceria surfaces, and therefore, considering that such vacancies strongly affect the oxidation state, packing motifs, and catalytic activity of supported metal clusters, they should be useful in the design of more efficient ceria-supported metal catalysts.

ACKNOWLEDGMENTS

Y.G. is supported by National Natural Science Foundation of China (11574340, 21773287) and CAS-Shanghai Science Research Center (CAS-SSRC-YJ-2015-01). M.V.G.-P. acknowledges support by the MINECO-Spain (CTQ2015-71823-R). The computational resources utilized in this research were provided by Shanghai Supercomputer Center, National Supercomputing Center in Tianjin and Shenzhen, and Special Program for Applied Research on Super Computation of the NSFC-Guangdong Joint Fund (the second phase) under Grant No. U1501501.

Z.-K.H. and Y.-Z.Y. contributed equally to this work.

[1] M. Dresselhaus and I. Thomas, Alternative energy technologies, Nature (London) **414**, 332 (2001).

[2] Q. Fu, H. Saltsburg, and M. Flytzani-Stephanopoulos, Active nonmetallic Au and Pt species on ceria-based water-gas shift catalysts, Science **301**, 935 (2003).

[3] G. Deluga, J. Salge, L. Schmidt, and X. Verykios, Renewable hydrogen from ethanol by autothermal reforming, Science **303**, 993 (2004).

[4] X. Wang, J. A. Rodriguez, J. C. Hanson, D. Gamarra, A. Martínez-Arias, and M. Fernández-García, In situ studies of

the active sites for the water gas shift reaction over Cu-CeO_2 catalysts: Complex interaction between metallic copper and oxygen vacancies of ceria, J. Phys. Chem. B **110**, 428 (2006).

[5] J. A. Rodriguez, S. Ma, P. Liu, J. Hrbek, J. Evans, and M. Pérez, Activity of CeO_x and TiO_x nanoparticles grown on Au(111) in the water-gas shift reaction, Science **318**, 1757 (2007).

[6] J. A. Rodriguez, P. Liu, J. Hrbek, J. Evans, and M. Pérez, Water gas shift reaction on Cu and Au nanoparticles supported on CeO_2(111) and ZnO(001): Intrinsic activity and importance of support interactions, Angew. Chem. Int. Ed. **119**, 1351 (2007).

[7] A. Bruix, J. A. Rodriguez, P. J. Ramírez, S. D. Senanayake, J. Evans, J. B. Park, D. Stacchiola, P. Liu, J. Hrbek, and F. Illas, A new type of strong metal–support interaction and the production of H_2 through the transformation of water on Pt/CeO_2(111) and Pt/CeO_x/TiO_2(110) catalysts, J. Am. Chem. Soc. **134**, 8968 (2012).

[8] M. Capdevila-Cortada, M. García-Melchor, and N. López, Unraveling the structure sensitivity in methanol conversion on CeO_2: A DFT+U study, J. Catal. **327**, 58 (2015).

[9] J. A. Farmer and C. T. Campbell, Ceria maintains smaller metal catalyst particles by strong metal-support bonding, Science **329**, 933 (2010).

[10] G. N. Vayssilov, Y. Lykhach, A. Migani, T. Staudt, G. P. Petrova, N. Tsud, T. Skála, A. Bruix, F. Illas, and K. C. Prince, Support nanostructure boosts oxygen transfer to catalytically active platinum nanoparticles, Nat. Mater. **10**, 310 (2011).

[11] C. Zhang, A. Michaelides, D. A. King, and S. J. Jenkins, Positive charge states and possible polymorphism of gold nanoclusters on reduced ceria, J. Am. Chem. Soc. **132**, 2175 (2010).

[12] C. Weststrate, R. Westerstrom, E. Lundgren, A. Mikkelsen, J. N. Andersen, and A. Resta, Influence of oxygen vacancies on the properties of ceria-supported gold, J. Phys. Chem. C **113**, 724 (2008).

[13] Z.-P. Liu, S. J. Jenkins, and D. A. King, Origin and Activity of Oxidized Gold in Water-Gas-Shift Catalysis, Phys. Rev. Lett. **94**, 196102 (2005).

[14] M. F. Camellone and S. Fabris, Reaction mechanisms for the CO oxidation on Au/CeO_2 catalysts: Activity of substitutional Au^{3+}/Au^+ cations and deactivation of supported Au^+ adatoms, J. Am. Chem. Soc. **131**, 10473 (2009).

[15] H. Y. Kim, H. M. Lee, and G. Henkelman, CO oxidation mechanism on CeO_2-supported Au nanoparticles, J. Am. Chem. Soc. **134**, 1560 (2012).

[16] Y. Zhou and J. Zhou, Interactions of Ni nanoparticles with reducible CeO_2(111) thin films, J. Phys. Chem. C **116**, 9544 (2012).

[17] P. G. Lustemberg, P. J. Ramírez, Z. Liu, R. A. Gutiérrez, D. G. Grinter, J. Carrasco, S. D. Senanayake, J. A. Rodriguez, and M. V. Ganduglia-Pirovano, Room-temperature activation of methane and dry re-forming with CO_2 on Ni-CeO_2(111) surfaces: Effect of Ce^{3+} sites and metal–support interactions on C–H bond cleavage, ACS Catal. **6**, 8184 (2016).

[18] P. Lustemberg, Y. Pan, B.-J. Shaw, D. Grinter, C. Pang, G. Thornton, R. Pérez, M. Ganduglia-Pirovano, and N. Nilius, Diffusion Barriers Block Defect Occupation on Reduced CeO_2(111), Phys. Rev. Lett. **116**, 236101 (2016).

[19] X. Wang, B. Chen, G. Chen, and X. Sun, Oxygen vacancies dependent Au nanoparticle deposition and CO oxidation, RSC Adv. **6**, 87978 (2016).

[20] J.-F. Jerratsch, X. Shao, N. Nilius, H.-J. Freund, C. Popa, M. V. Ganduglia-Pirovano, A. M. Burow, and J. Sauer, Electron Localization in Defective Ceria Films: A Study with Scanning-Tunneling Microscopy and Density-Functional Theory, Phys. Rev. Lett. **106**, 246801 (2011).

[21] D. C. Grinter, R. Ithnin, C. L. Pang, and G. Thornton, Defect structure of ultrathin ceria films on Pt (111): Atomic views from scanning tunnelling microscopy, J. Phys. Chem. C **114**, 17036 (2010).

[22] Y. Namai, K.-I. Fukui, and Y. Iwasawa, Atom-resolved noncontact atomic force microscopic and scanning tunneling microscopic observations of the structure and dynamic behavior of CeO_2(111) surfaces, Catal. Today **85**, 79 (2003).

[23] H. Nörenberg and G. Briggs, Defect Structure of Nonstoichiometric CeO_2(111) Surfaces Studied by Scanning Tunneling Microscopy, Phys. Rev. Lett. **79**, 4222 (1997).

[24] F. Esch, S. Fabris, L. Zhou, T. Montini, C. Africh, P. Fornasiero, G. Comelli, and R. Rosei, Electron localization determines defect formation on ceria substrates, Science **309**, 752 (2005).

[25] Y. Namai, K.-i. Fukui, and Y. Iwasawa, Atom-resolved noncontact atomic force microscopic observations of CeO_2(111) surfaces with different oxidation states: Surface structure and behavior of surface oxygen atoms, J. Phys. Chem. B **107**, 11666 (2003).

[26] S. Gritschneder, Y. Namai, Y. Iwasawa, and M. Reichling, Structural features of CeO_2(111) revealed by dynamic SFM, Nanotechnology **16**, 41 (2005).

[27] S. Torbrügge, M. Reichling, A. Ishiyama, S. Morita, and O. Custance, Evidence of Subsurface Oxygen Vacancy Ordering on Reduced CeO_2(111), Phys. Rev. Lett. **99**, 056101 (2007).

[28] R. Olbrich, G. E. Murgida, V. Ferrari, C. Barth, A. M. Llois, M. Reichling, and M. V. Ganduglia-Pirovano, Surface stabilizes ceria in unexpected stoichiometry, J. Phys. Chem. C **121**, 6844 (2017).

[29] N. Skorodumova, M. Baudin, and K. Hermansson, Surface properties of CeO_2 from first principles, Phys. Rev. B **69**, 075401 (2004).

[30] Y. Jiang, J. B. Adams, and M. Van Schilfgaarde, Density-functional calculation of CeO_2 surfaces and prediction of effects of oxygen partial pressure and temperature on stabilities, J. Chem. Phys. **123**, 064701 (2005).

[31] M. Nolan, S. C. Parker, and G. W. Watson, The electronic structure of oxygen vacancy defects at the low index surfaces of ceria, Surf. Sci. **595**, 223 (2005).

[32] S. Fabris, G. Vicario, G. Balducci, S. de Gironcoli, and S. Baroni, Electronic and atomistic structures of clean and reduced ceria surfaces, J. Phys. Chem. C **109**, 22860 (2005).

[33] C. Zhang, A. Michaelides, D. A. King, and S. J. Jenkins, Oxygen vacancy clusters on ceria: Decisive role of cerium f electrons, Phys. Rev. B **79**, 075433 (2009).

[34] M. V. Ganduglia-Pirovano, J. L. F. Da Silva, and J. Sauer, Density-Functional Calculations of the Structure of Near-Surface Oxygen Vacancies and Electron Localization on CeO_2(111), Phys. Rev. Lett. **102**, 026101 (2009).

[35] H.-Y. Li, H.-F. Wang, X.-Q. Gong, Y.-L. Guo, Y. Guo, G. Lu, and P. Hu, Multiple configurations of the two excess 4f electrons on defective CeO_2(111): Origin and implications, Phys. Rev. B **79**, 193401 (2009).

[36] H.-Y. Li, H.-F. Wang, Y.-L. Guo, G.-Z. Lu, and P. Hu, Exchange between sub-surface and surface oxygen vacancies on

CeO_2(111): A new surface diffusion mechanism, Chem. Commun. **47**, 6105 (2011).

[37] J. C. Conesa, Surface anion vacancies on ceria: Quantum modelling of mutual interactions and oxygen adsorption, Catal. Today **143**, 315 (2009).

[38] A. P. Amrute, C. Mondelli, M. Moser, G. Novell-Leruth, N. López, D. Rosenthal, R. Farra, M. E. Schuster, D. Teschner, T. Schmidt, and J. Pérez-Ramírez, Performance, structure, and mechanism of CeO_2 in HCl oxidation to Cl_2, J. Catal. **286**, 287 (2012).

[39] J. J. Plata, A. M. Márquez, and J. F. Sanz, Transport properties in the CeO_{2-x}(111) surface: From charge distribution to ion-electron collaborative migration, J. Phys. Chem. C **117**, 25497 (2013).

[40] G. E. Murgida and M. V. Ganduglia-Pirovano, Evidence for Subsurface Ordering of Oxygen Vacancies on the Reduced CeO_2(111) Surface Using Density-Functional and Statistical Calculations, Phys. Rev. Lett. **110**, 246101 (2013).

[41] Z. Yang, T. K. Woo, M. Baudin, and K. Hermansson, Atomic and electronic structure of unreduced and reduced CeO_2 surfaces: A first-principles study, J. Chem. Phys. **120**, 7741 (2004).

[42] Z.-K. Han, Y.-G. Wang, and Y. Gao, Catalytic role of vacancy diffusion in ceria supported atomic gold catalyst, Chem. Commun. **53**, 9125 (2017).

[43] Z.-K. Han and Y. Gao, A 2D–3D structure transition of gold clusters on CeO_{2-x}(111) surfaces and its influence on CO and O_2 adsorption: A comprehensive DFT+ U investigation, Nanoscale **7**, 308 (2015).

[44] J. Kullgren, M. J. Wolf, C. Castleton, P. Mitev, W. Briels, and K. Hermansson, Oxygen Vacancies versus Fluorine at CeO_2(111): A Case of Mistaken Identity? Phys. Rev. Lett. **112**, 156102 (2014).

[45] X.-P. Wu and X.-Q. Gong, Clustering of Oxygen Vacancies at CeO_2(111): Critical Role of Hydroxyls, Phys. Rev. Lett. **116**, 086102 (2016).

[46] M. J. Wolf, J. Kullgren, and K. Hermansson, Comment on "Clustering of Oxygen Vacancies at CeO_2(111): Critical Role of Hydroxyls," Phys. Rev. Lett. **117**, 279601 (2016).

[47] X.-P. Wu and X.-Q. Gong, Wu and Gong Reply, Phys. Rev. Lett. **117**, 279602 (2016).

[48] J. Kullgren, M. J. Wolf, P. D. Mitev, K. Hermansson, and W. J. Briels, DFT-Based Monte Carlo simulations of impurity clustering at CeO_2(111), J. Phys. Chem. C **121**, 15127 (2017).

[49] J. P. Perdew, K. Burke, and M. Ernzerhof, Generalized Gradient Approximation Made Simple, Phys. Rev. Lett. **77**, 3865 (1996).

[50] G. Kresse and J. Furthmüller, Efficient iterative schemes for *ab initio* total-energy calculations using a plane-wave basis set, Phys. Rev. B **54**, 11169 (1996).

[51] S. Dudarev, G. Botton, S. Savrasov, C. Humphreys, and A. Sutton, Electron-energy-loss spectra and the structural stability of nickel oxide: An LSDA+U study, Phys. Rev. B **57**, 1505 (1998).

[52] M. Cococcioni and S. de Gironcoli, Linear response approach to the calculation of the effective interaction parameters in the LDA+U method, Phys. Rev. B **71**, 035105 (2005).

[53] C. Castleton, J. Kullgren, and K. Hermansson, Tuning LDA+U for electron localization and structure at oxygen vacancies in ceria, J. Chem. Phys. **127**, 244704 (2007).

[54] G. Kresse and D. Joubert, From ultrasoft pseudopotentials to the projector augmented-wave method, Phys. Rev. B **59**, 1758 (1999).

[55] See Supplemental Material at http://link.aps.org/supplemental/10.1103/PhysRevMaterials.2.035802 for structural models of different types of near-surface oxygen vacancies at the reduced CeO_2(111) surface and oxygen vacancy formation energies for the multiple configurations of the excess charge, details of the Monte Carlo simulations, as well as structures and simulated STM images of vacancy structures according to the F-impurity and hydroxyl-vacancy models.

[56] J. Tersoff and D. Hamann, Theory of the scanning tunneling microscope, in *Scanning Tunneling Microscopy* (Springer, Berlin, 1985), Vol. 59.

[57] M. Troppenz, S. Rigamonti, and C. Draxl, Predicting ground-state configurations and electronic properties of the thermoelectric clathrates $Ba_8Al_xSi_{46-x}$ and $Sr_8Al_xSi_{46-x}$, Chem. Mater. **29**, 2414 (2017).

[58] N. Metropolis, A. W. Rosenbluth, M. N. Rosenbluth, A. H. Teller, and E. Teller, Equation of state calculations by fast computing machines, J. Chem. Phys. **21**, 1087 (1953).

[59] Y. Pan, N. Nilius, H.-J. Freund, J. Paier, C. Penschke, and J. Sauer, Titration of Ce^{3+} Ions in the CeO_2(111) Surface by Au Adatoms, Phys. Rev. Lett. **111**, 206101 (2013).

[60] M. Capdevila-Cortada and N. López, Entropic contributions enhance polarity compensation for CeO_2(100) surfaces, Nat. Mater. **16**, 328 (2016).

[61] D. A. Andersson, S. I. Simak, N. V. Skorodumova, I. A. Abrikosov, and B. Johansson, Optimization of ionic conductivity in doped ceria, Proc. Natl. Acad. Sci. **103**, 3518 (2006).